Cavitation and structural analysis on a flanged diffuser applied to hydrokinetic turbines

Yves Alexandrino Bandeira[1] [iD], Leonardo Dantas Rodrigues[1] [iD],
Jerson Rogério Pinheiro Vaz[1] [iD], Erb Ferreira Lins[2] [iD]

[1]Universidade Federal do Pará, Programa de Pós-Graduação em Engenharia Mecânica. Rua Augusto Corrêa, 01, 66075-110, Belém, PA, Brasil.

[2]Universidade Federal Rural do Pernambuco, Unidade Acadêmica do Cabo de Santo Agostinho. Rua Cento e Sessenta e Três, 300, 54518-430, Cabo de Santo Agostinho, PE, Brasil.

e-mail: yves.bandeira@itec.ufpa.br, leodr@ufpa.br, jerson@ufpa.br, erb.lins@ufrpe.br

ABSTRACT

Flanged diffuser can improve hydrokinetic turbine efficiency. However, in the current literature it is still not clear if the flange allows the possibility of cavitation on its structure, and whether it can support high pressure variation. This work presents a Computational Fluid Dynamics (CFD) study on the effect of cavitation on a flanged diffuser. The water flow through the diffuser was evaluated using a Reynolds Averaged Navier Stokes approach coupled to the Rayleigh-Plesset model to estimate the vapor production rate. The methodology was applied to a flanged diffuser and results were compared with experimental data from the literature. The minimal depth to avoid cavitation on the flanged diffuser was found. The pressure field obtained on CFD was applied as loading in structural analysis using Finite Element Method. The numerical model presented good agreement with experimental data available in the literature. The results showed that cavitation occurs more intensely at a depth of 1.0 m for the model. This intensity gradually decreases as the depth increases. Cavitation can be present in flanged diffusers, especially in the region inside the shroud, where it can directly impact the flow through the rotor. A good safety factor was obtained in the structural analysis.

Keywords: Cavitation; Flanged Diffuser; Rayleigh-Plesset model; Computational Fluid Dynamics; Fluid-Structural interaction.

1. INTRODUCTION

The use of hydrokinetic energy is one of the most promising alternatives among the renewable energy options. In this type of energy harvesting, water currents are used as a source of power. The energy that can be extracted from water flows is about 1000 times greater than the air current with the same velocity, since the generated power is proportional to fluid density, which leads to turbine rotors with smaller diameters. Also, the flow of rivers and ocean tides are steadier, giving this source more predictability of power output when compared with wind and solar sources. Despite the huge amounts of available energy, this type of renewable source is barely exploited. One of the drawbacks is usually lower flow velocity in water currents, which requires more studies to optimize the turbine for this situation [1].

One of the alternatives to increasing the power output is to use a diffuser or a duct to increase the flow velocity at the rotor. In this context, the flanged diffuser has recently attracted considerable attention as it can achieve a high power coefficient [2]. However, when the diffuser is immersed in water, it is subjected to hydrodynamic forces. These forces change over time due to vortex shedding, turbine interaction, boundary layer detachment and reattachment etc. When the diffuser is not optimized to reduce these forces, the loads tend to be higher. Also, in the current literature, it is still not clear if the flange allows the possibility of cavitation on its structure, and whether it can support high pressure variation. As observed in [3], one important factor to turbine performance is the expansion area ratio. This expansion can lead to flow separation in the inner wall of diffuser. That will cause a negative effect on performance and could also lead to cavitation. It is important to note that in flanged diffusers applied in hydrokinetic turbines, the pressure load can cause high levels of stress due to the bending, especially at the intersection of the flange with the tubular part of the diffuser. In this sense, studies of fluid-structure interaction are fundamental to guiding the structural design of this component.

Some studies have already investigated into cavitation in hydrokinetic turbines with diffusers. In [4], a study of cavitation was done, but the analysis was restricted to turbine blades, where it was found that the presence of a shroud increases the possibility of cavitation on the blades. An optimization technique, which changes the chord and twist angle distributions, was also proposed to reduce this effect, and the results show that the optimization keeps the efficiency of the turbine higher. In [5], an approach for optimizing hydrokinetic blades free of cavitation under diffuser effect was proposed. The model used the minimum pressure coefficient as a criterion to keep the pressure near blade tip above water vapor pressure. But it did not study the cavitation on the diffuser, only on the blade. In [6] a new optimization procedure applied to hydrokinetic turbine swept blades was developed, with the main objective being the design of blades with reduced axial load on the rotor and possible reduction of the cavitation on blade tip. The approach demonstrated good result to reduce cavitation on hydrokinetic blades, however, any study on diffuser under cavitating condition was made. In [7], a study of the expansion angle, length, height, and load factor of flanged diffuser of a wind turbine was done. This work used Computational Fluid Dynamics methodology to evaluate the pressure zones in front and behind the diffuser and its relation to flange height. It is found that higher heights increase the pressure difference and the flow velocity inside the diffuser.

The aerodynamic loads at the diffuser were studied in [8], where a novel, self-adaptative flanged diffuser was proposed. The work uses a CFD approach and found out that about 69% of the load at a shrouded wind turbine are caused by the loads in the diffuser. By changing the flange to a flexible structure, authors can predict a reduction of about 35% of the load at high wind velocities. With the aim of reducing drag and optimizing efficiency of a diffuser augmented wind turbine, in [9] an optimization framework was established using a CFD solver, a mesh morphing technique and a differential evolution algorithm, to modify and optimize the diffuser geometry to simultaneously reduce the drag of the wind turbine and keep the acceleration in plane rotor at maximum, thus increasing power output. The methodology was applied to optimize the diffuser of a 15 kW wind turbine and achieves a 42% drag reduction, a 1.86 velocity speed-up and a volume reduction of 42%, allowing even smaller costs in the construction of this component.

Although there are several works available in the current literature on diffusers, the authors are unaware of any study on cavitation and its hydrodynamic effect on the structure of a flanged diffuser. Hence, in the present work, a study of the hydro flow around a flanged diffuser is done to evaluate the forces on its structure and the flow cavitation possibility. A Finite volume RANS solver is used to compute the velocity and pressure fields, and the hydrodynamic load on the flange is transferred to a Finite Element Solver, where the stresses in the diffuser are computed. The flow is considered as a two phases continuous mixture of liquid water and vapor, where the mass transfer between phase is computed using the Rayleigh-Plesset Model. Results for cavitation analysis are obtained at 3 different immersion depths and, for stress evaluation, 6 different flange thicknesses. Such results demonstrate that cavitation appears on flanged diffusers, especially in the region inside the shroud, where it can directly impact the flow through the rotor. Also, as the drag can induce high levels of stresses on the flange, it is needed attention when this structure is built.

2. NUMERICAL MODEL FOR THE CAVITATING FLOW SIMULATION

To obtain forces at the hydrokinetic diffuser and to investigate the presence of cavitation, a numerical modeling using Computational Fluid Dynamics (CFD) is used in the present study to simulate the flow throughout the rotor. The CFD technique is a good tool for this purpose, since it can predict accurately the flow over the rotor blade, allowing the evaluation of the cavitation constraint introduced into the turbine thrust coefficient. In this section, we describe the numerical parameters and models used in the simulation.

The flow through the turbine rotor is assumed to be incompressible and fully turbulent. Consequently, velocity and pressure fields are governed by the Navier-Stokes equations. The approach assumes flow as being statistically stationary. In this sense, the simulations provide timed averaged velocity and pressure fields around the rotor blades and the diffuser. To consider the turbulent phenomena, without numerically solving all the eddy scales, the Reynolds Averaged Navier-Stokes (RANS) approach is adopted. This technique has been commonly used to simulate Turbo machinery flow [10] and currently RANS evolved to a standard in the accurate prediction of free flow turbines performance [11]. In RANS methodology, the contribution of the turbulent pressures and velocity fluctuations (u'_i and p', respectively) to the temporal average velocity and pressure fields is given by the Reynolds Stress Tensor $\tau_{ij} = \overline{u'_i u'_j}$, which must be modeled. In the present work, the $\kappa - \omega$ Shear-Stress Transport (SST) model is employed [12].

To verify if the cavitation is present, the simulations of flows are performed considering a two-phase continuum mixture of liquid water and vapor. In this case, the phase continuity equations can be written as

$$\frac{\partial r_\alpha \rho_\alpha}{\partial t} + \frac{\partial r_\alpha \rho_\alpha u_i}{\partial x_i} = \dot{m}_\alpha \qquad (1)$$

where u_i are the components of mean velocity field, ρ is the density and $\dot{m}_\alpha$ represents the rate of change of mass for each phase, per unit of mixture volume. These source terms account for mass exchange between the vapor and liquid phases. The subscript $\alpha = (l,v)$ represents the liquid and vapor phases and r_α is the volume fraction of each one. Considering that $r_l + r_v = 1$ the mass conservation principle requires that

$$\dot{m}_v = -\dot{m}_i \tag{2}$$

Assuming that both phases have the same velocity, the mean momentum conservation equation is modified only by changing the fluid density ρ by the mixture density $\rho_m = \rho_l r_l + \rho_v r_v$, in such a way that

$$\rho_m \frac{\partial u_j}{\partial t} + \rho_m\, u_i\, \frac{\partial u_j}{\partial x_i} = -\frac{\partial p}{\partial x_j} + \frac{\partial}{\partial x_i}(2\mu S_{ij} - \rho_m \overline{u_i' u_j'}) + \rho_m f_i \tag{3}$$

where p is the mean pressure, μ is the dynamic viscosity, f_i is a force per unit of volume in direction i, which may represent the gravitational, Coriolis and centrifugal contributions and S_{ij} are the components of the symmetric part of the velocity gradient tensor. As previously mentioned, the Reynolds Stress Tensor $\overline{u_i' u_j'}$ is modeled by the Boussinesq' hypotheses and the $\kappa - \omega - \text{SST}$ model.

Equation 2 allows the two-phase calculations to be done by solving only one differential continuity equation in addition to the momentum equation, written in the form of Equation 3. To proceed in this manner, an equation for the mass source term $\dot{m}_v$ is required, which may be derived from the so-called Rayleigh-Plesset model [13] for a spherical vapor bubble

$$R_B \frac{d^2 R_B}{dt^2} + \frac{3}{2}\left(\frac{dR_B}{dt}\right)^2 + \frac{2\sigma s}{\rho_l R_B} = \frac{p_v - p}{\rho_l}, \tag{4}$$

where R_B is the bubble radius, σ_s is the surface tension coefficient and p_v is the pressure in the bubble, assumed to be the vapor pressure at the liquid temperature. Assuming that only large bubbles are important in cavitation, the second order terms and the surface tension are very small and can be neglected when compared with the pressure difference [14]. After these simplifications, Equation 4 reduces to

$$\frac{dR_B}{dt} = \sqrt{\frac{2}{3}\frac{p_v - p}{\rho_l}} \tag{5}$$

Defining the bubble density number, N_B, as being the number of bubbles per unit of volume of the mixture, the rate of change of vapor mass per unit of volume can be calculated by

$$\dot{m}_v = N_B \rho_v 4\pi R_B^2 \sqrt{\frac{2}{3}\frac{p_v - p}{\rho_l}} \tag{6}$$

Additionally, $r_v = N_B 4\pi R_B^3/3$, in such a way we can rewrite Equation 6 in terms of the fraction of vapor in the form

$$\dot{m}_v = \frac{3V_v \rho_v}{R_B}\sqrt{\frac{2}{3}\frac{p_v - p}{\rho_l}} \tag{7}$$

Equation 7 relates the mass exchanging rate between phases to the square root of the difference between the vapor pressure inside the bubble and local mechanical pressure. In this form, the cavitation model is restricted only to vaporization, *i.e.,* $\dot{m}_v > 0$, because $p_v - p$ must be positive. In other words, Equation 7 cannot handle a radius decrease ($dR_B / dt < 0$) due to condensation, which takes place inside the bubble when $p > p_v$. In addition, the original Rayleigh-Plesset model does not consider nucleation phenomena. Vaporization begins at nucleation sites and, as the vapor volume fraction increases, the nucleation site density decreases. Thus, only for vaporization, r_v is replaced by $r_{nuc}(1 - r_v)$, where r_{nuc} is the volume fraction of the nucleation sites [15, 16] propose a heuristic modification that, together with nucleation accounting, leads to Equation 8, where F_c is an empirical constant used to discriminate condensation and vaporization. In that work, a numerical calibration was

done using experimental data [17, 18], and found that $F_c = 50$ for vaporization and $F_c = 0.01$ for condensation accurately reproduces leading edge and mid-chord hydrofoil cavitation. The values of parameters in Equation 8 found in [16] are given in Table 1.

$$\dot{m}_v = F_c \frac{3 r_{nuc}(1-r_v)\rho_v}{R_B} \sqrt{\frac{2}{3} \frac{|p_v - p|}{p_l}} sign(p_v - p) \tag{8}$$

2.1. Numerical setup

The geometric model was constructed based on works such as [19] and [20]. Figure 1 shows the diffuser dimensions, where $D, L = 1.5D, \phi = 4°$ and $h = D/2$, denote diffuser diameter at the inlet, length, opening angle and height of flange, respectively. An immersion depth H was considered. A numerical solution was performed using ANSYS CFX 18.1 [21] for simulated a flow through the diffuser. The computational domain consists of a cylinder with diameter of $20D$ and length of $15D$. The diffuser is positioned at a distance of $5D$ from the inlet boundary and $8.5D$ from outlet, to avoid any influence of the inlet and outlet sections. To simplify the simulation process, only 1/8 of the domain was used. In this way, it was possible to refine more precisely the flow zones that most influence the flow velocity through the diffuser. The refinement covered a region from $–0.5D$ to $2.4D$ from the diffuser inlet, as shown in Figure 2.

Table 2 shows the boundary condition applied. At inlet, a uniform velocity field of 5 m/s and 5% turbulence intensity was applied. At the outlet, a zero-pressure condition was considered. The non-slip condition was applied at the diffuser surfaces, while the free slip condition was applied at the top and lateral surfaces. periodicity shows these boundary conditions applied to domain surfaces. Only 1/8 of the domain was simulated, with periodic conditions applied in lateral surfaces. The domain boundary surfaces are show in Figure 3.

Table 1: Material constants and general conditions for the Rayleigh-Plesset Model at 25°C.

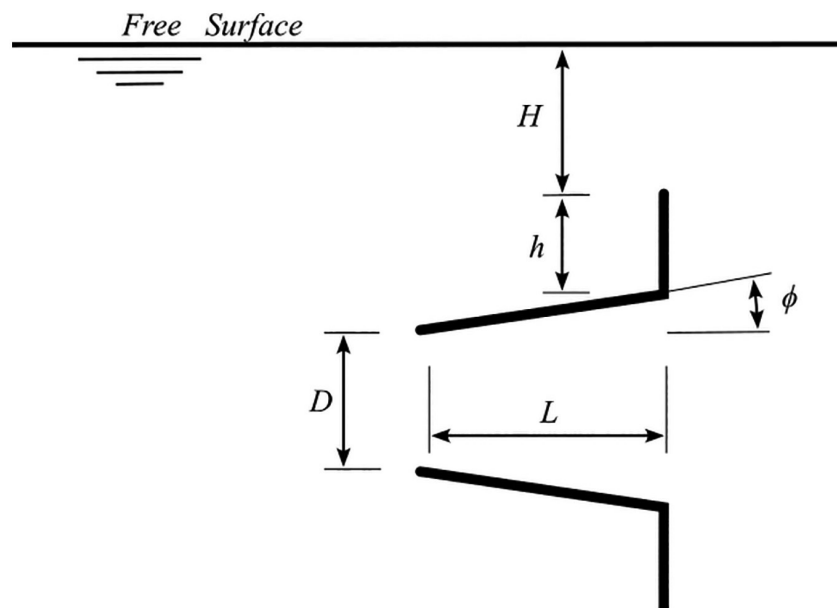| PARAMETER	VALUE
F_c	0.01 (Condensation) and 50 (Vaporization)
ρ_l	997 kg/m³
ρ_v	0.02308 kg/m³
r_{nuc} [13]	5×10^{-4} m
Mean bubble diameter (R_B) [13]	1×10^{-6} m
Reference pressure (p_∞)	109.78, 119.56, and 129.34 kPa
Vapor pressure (p_v)	3.170 kPa

Figure 1: Schematic view of the flanged diffuser cross section and installation setup.
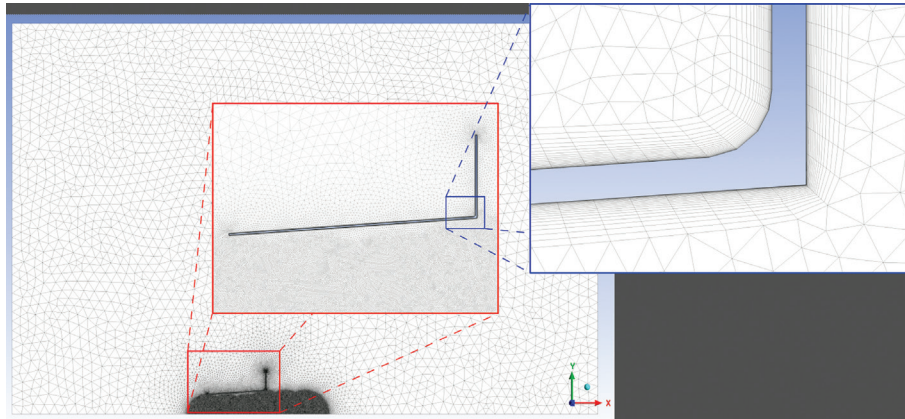
Figure 2: Mesh details with refinement on the wall and in the internal region of the diffuser.

Table 2: Boundary conditions applied in the domain surfaces.

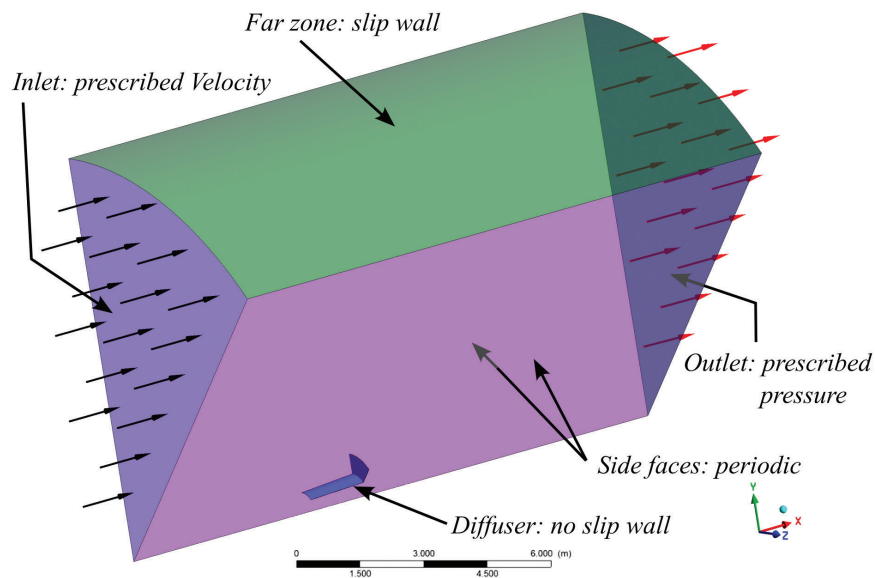| REGION	CONDITION
Inlet	Prescribed velocity $u = U_\infty = 5m/s$
	Turbulence intensity 5%
Outlet	Prescribed pressure $p = 0Pa$
Diffuser surface	Non-slip wall
Domain side faces	Periodicity
Top (Far zone)	Free slip wall

Figure 3: Domain surfaces and boundary conditions applied.

3. RESULTS AND DISCUSSION

3.1. Numerical validation

For the numerical validation, the convergence of results is assessed using four mesh refinement levels, and then the selected grid is compared with data in reference. The axial normalized velocity along the center line of domains is shown in Figure 4. The main difference occurs at the peak in which the coarsest and finest mesh differ about 1.67%. Comparing with experimental data [19], despite of this difference found, the selected grid can capture the variation of the velocity. The increase on axial velocity is clearly noted, and the local velocity increases 1.61 times the inlet velocity (U_∞).

Along with this the mesh study, it is necessary to observe the turbulent viscosity ratio in the boundary layer and analyze whether the mesh is suitable for the $\kappa - \omega - SST$ turbulence model. In Fig. 5, the turbulent viscosity ratio along the prismatic layer is plotted. A large increase in the viscosity ratio is observed, where the maximum value occurs near the middle of the boundary layer, returning to the minimum value still within the prismatic layer. This is the behaviour expected when a suitable mesh distribution is correctly set to $\kappa - \omega - SST$ turbulence model.

3.2. Operating conditions

Once the numerical parameters are defined, the next step was to perform the cavitation analysis. Within the basic configurations of the ANSYS CFX, the fluid was defined as water and water vapor, both at 25°C. After that, the option of mass transfer for cavitation was defined in the Rayleigh-Plesset model. Then, general conditions were defined such as condensation, vaporization, average bubble diameter, vapor pressure etc. Table 4 shows the values of such conditions. Finally, the inlet velocity was adjusted to 2.5 m/s, according to previous studies of cavitation and fatigue in hydrokinetic turbines done in [20, 22, 23], and the reference pressure was changed according to the depths chosen to perform the simulations.

3.3. Cavitating flow on the flanged diffuser

A diffuser with $D = 10$ m was analyzed, similarly to the work done by [20] and [23]. However, the analysis was performed for three different submersion levels (H), while in the cited works only one depth level was used. The pressure and velocity fields and the vapor volume fraction were calculated. Cavitation arises when the pressure
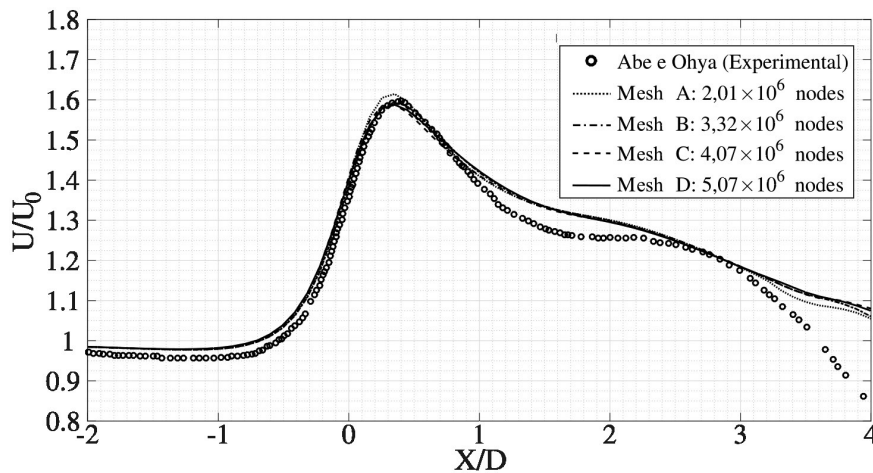

Figure 4: Comparison of axial velocity at center of domain obtained by the CFD model with the experimental measurements of [19].
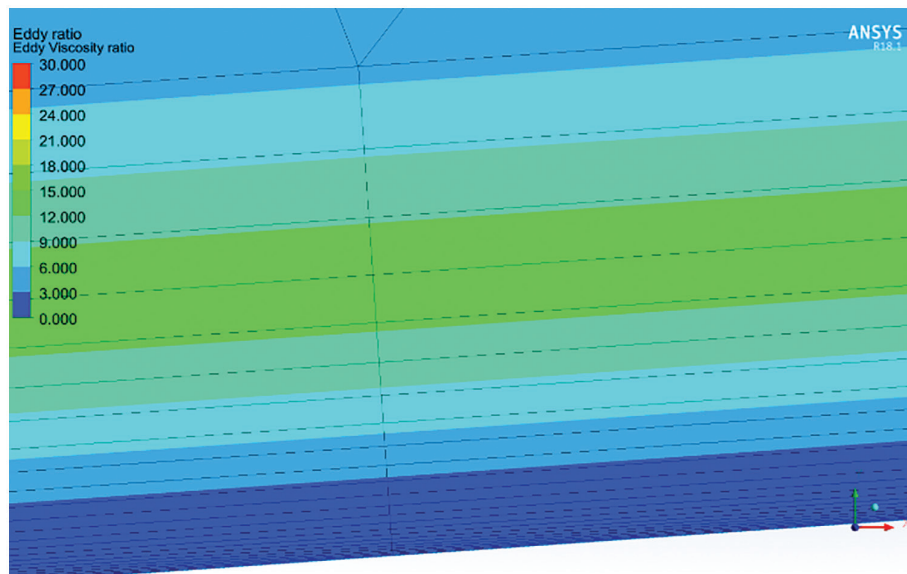

Figure 5: Prismatic layers correctly adapted for the $\kappa - \omega - SST$ representation of boundary layer. In this plot, $y^+_{max} = 0.987$.

**Table 3:** Mesh sensibility study.

MESH	NODES [×10⁶]	y^+_{max}	LAYERS	HIGHEST VELOCITY MAGNITUDE	RELATIVE ERROR [%]
Mesh A	2.01	1.025	25	1.615	0.91
Mesh B	3.32	0.987	25	1.594	0.35
Mesh C	4.07	0.980	25	1.588	0.74
Mesh D	5.07	0.998	25	1.588	0.77

Table 4: Design parameters used in the present simulation.

PARAMETERS	VALUES
Flow Velocity (U_∞)	2.5 m/s
Water density (ρ) 25°C at	997 kg/m³
Diffuser depth (H)	1, 2, and 3 m
P_{atm}	1×10^5 Pa
P_v	3.17×10^3 Pa
Gravity acceleration (g)	9.81 m/s²
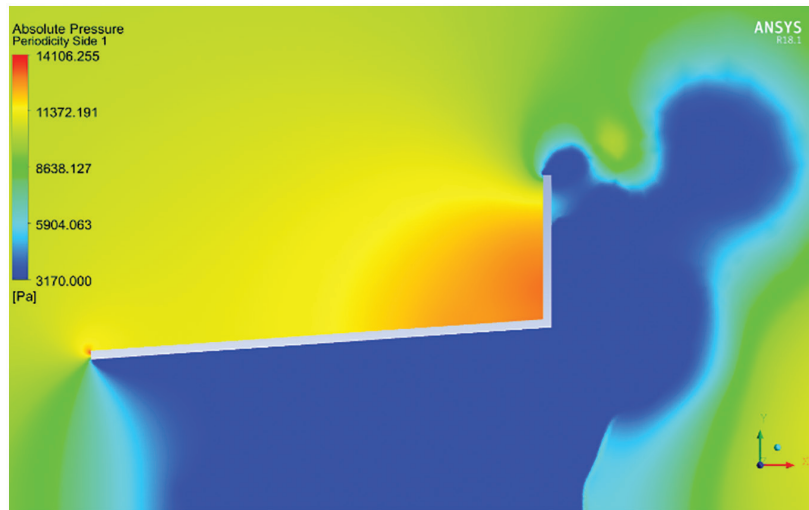
(a)
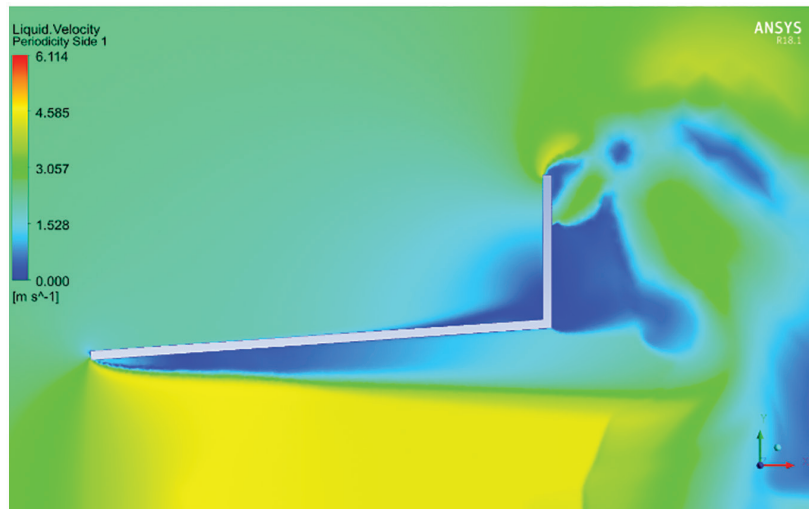
(b)

Figure 6: Pressure (a) and velocity magnitude (b) fields on the flanged diffuser for $H = 1.0$ m depth.

drops below the vapor pressure. This can be detected not only by the vapor volume fraction field, but also by analyzing the pressure values.

Analyzing the pressure field in Figure 6a for submersion of m, it was noted that there is a pressure drop inside the diffuser and just behind the flange, suggesting a high possibility of cavitation. Comparing with the velocity field of Figure 6b, an increase in velocity was observed in the inner part. It can be also observed that there was a detachment of the flow in internal wall of the diffuser. In Figure 7, it can be seen the total pressure of the flow over the surface of the diffuser. This information will be used in next section to compute the structural load in this component.

According to the work of [20], the total vapor volume is used to quantify cavitation. Thus, the presence of cavitation effect is considered only when the volume fraction is greater than 0.01. Figure 8a shows the cavitation effect inside the diffuser, with bubble formation starting at the entrance of diffuser and propagating in the direction flow. Figure 8b illustrates the cavitation on the upper part of the diffuser flange, where there was a large formation of bubbles, and it is also possible to observe this effect on the rear part of the flange. Both to a depth of m measured from the free surface of the water to the flange. In this operating condition, the vapor volume fraction intensifies due to the local hydraulic pressure being lower than the water vapor pressure. Such an effect can be mitigated with an increase in the diffuser depth.

When analyzing the pressure field of Fig. 9a, there was an increase in hydraulic pressure due to the higher depth level. However, regions where the liquid pressure is below the vapor pressure decreased, in such a way that it can be considered that the cavitation effect will also be smaller in the respective region. In Fig. 9b, a certain discontinuity in the flow was observed inside the diffuser. This discontinuity occurs due to the detachment of inner boundary layer. It is possible to see in Fig. 10a that there was a gradual decrease in the cavitation effect in the internal region of the diffuser, with the formation of bubbles more concentrated in the part closest to diffuser entrance, but still with cavitation. Fig. 10b shows that cavitation in the diffuser flange does not occur for a depth level of $H = 2.0$ m.

Figure 11a shows that for $H = 3.0$ m the pressures showed smaller pressures. It can be seen in Fig. 11b that there is a decrease in the region where the velocity is maximum, and a slightly more continuous flow compared to Fig. 10b. It was verified in Fig. 12 that the vapor volume fraction values are well below 0.01, that is, there is no cavitation on the diffuser surface in this depth.

3.4. Structural analysis of the flanged diffuser

To assess the structural response of the flanged diffuser, the pressure field obtained in the flow analysis at $H = 3$ m is used to compute the structural loads. The necessary thickness to avoid possible structural failures, especially on the flange, is then evaluated. The model is also made with 1/8 symmetry, as it is in the flow model. A mesh convergence analysis is carried out with reference to the stresses at the junction of the flange with the cylindrical part of the diffuser, having a final mesh with 27811 elements, corresponding to elements with a size of 10% of
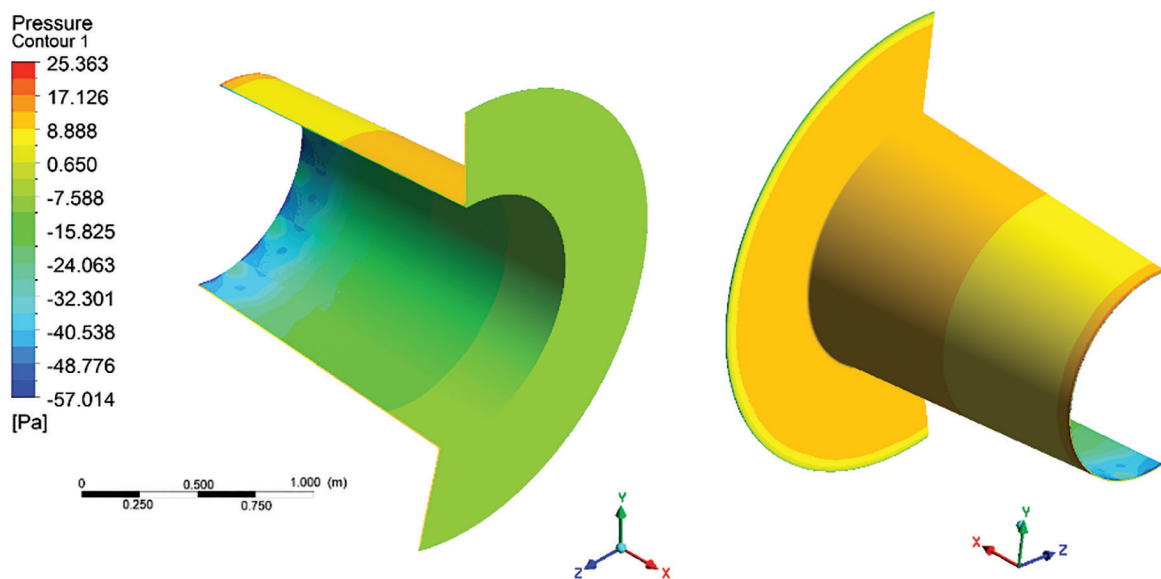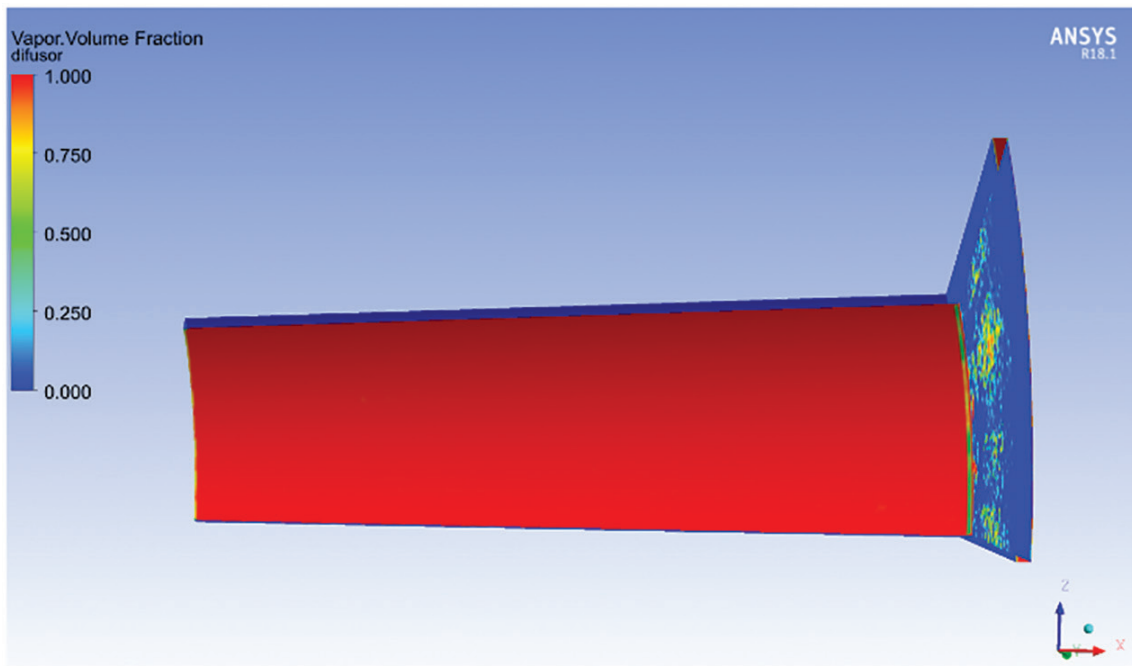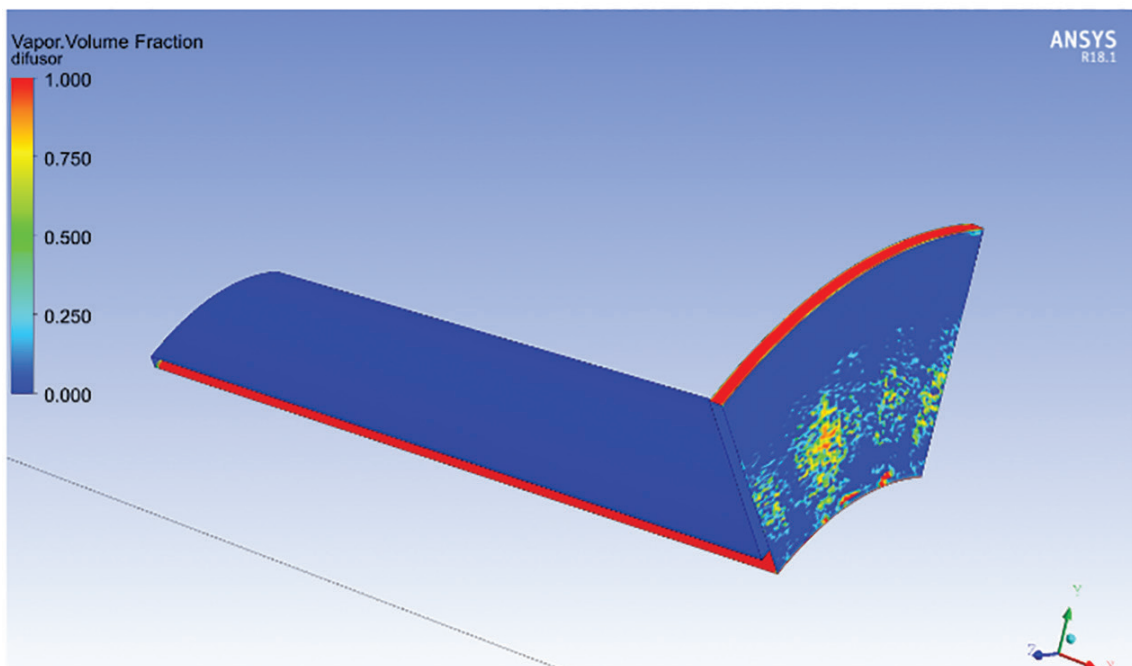

Figure 7: Pressure at diffuser surface for $H = 1.0$ m depth.

Figure 8: Volume fraction of vapor on diffuser inner part (a), and on the flange (b) for $H = 1.0$ m depth.

the thickness in the critical zone. Figure 13 shows the imposed boundary and symmetry conditions. Figure 14 shows detail in the critical zone of final mesh.

Four different thicknesses are analyzed using the aluminum alloy parameters, with a yield limit of 280 Mpa, a density of 2770 kg/m^3, a Young's modulus of 71 Gpa, a shear modulus of 26 Gpa and a Poisson's ratio of 0.33. Table 5 shows stress and safety factor (ratio between the yield limit and the von Mises stress at the

(a)
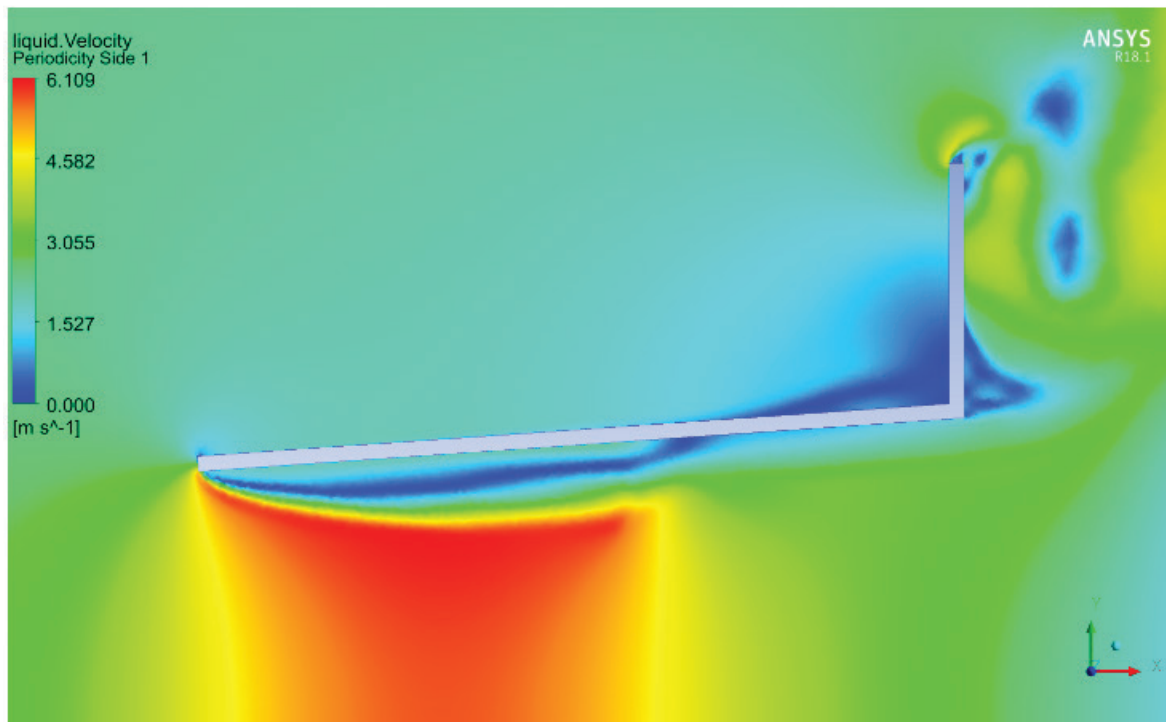
(b)

Figure 9: Pressure (a) and velocity magnitude (b) fields on the flanged diffuser for $H = 2.0$ m depth.

critical point) for four different thicknesses and the fillet radius for 7 mm thickness. This criterion is only met for thicknesses above 6 mm. When analyzing Equivalent von-Mises Stress on the diffuser with 7 mm thickness, shown in Fig. 15, the region that demands more attention is the flange, where the stresses are much higher than those of the cylindrical part.
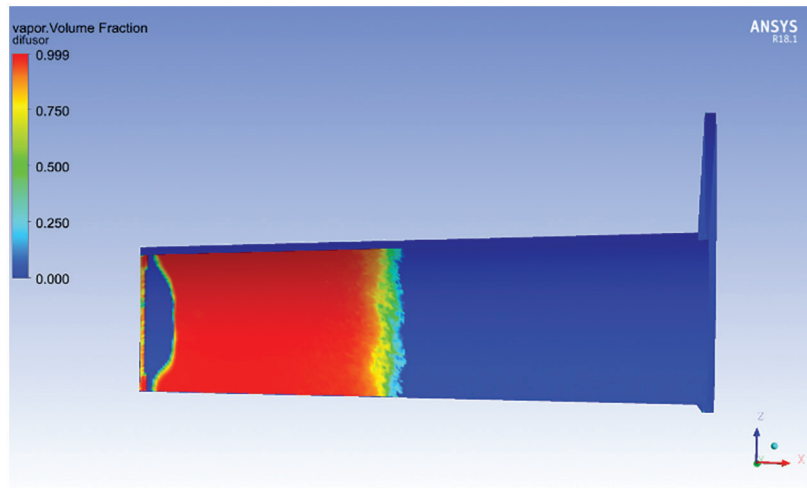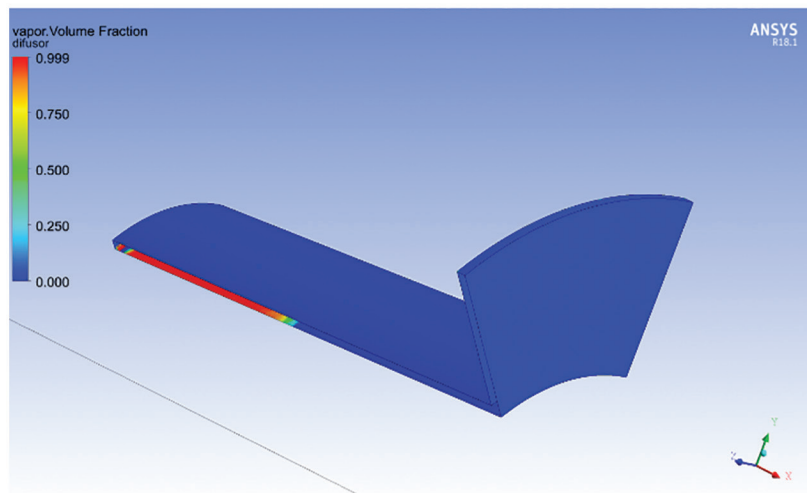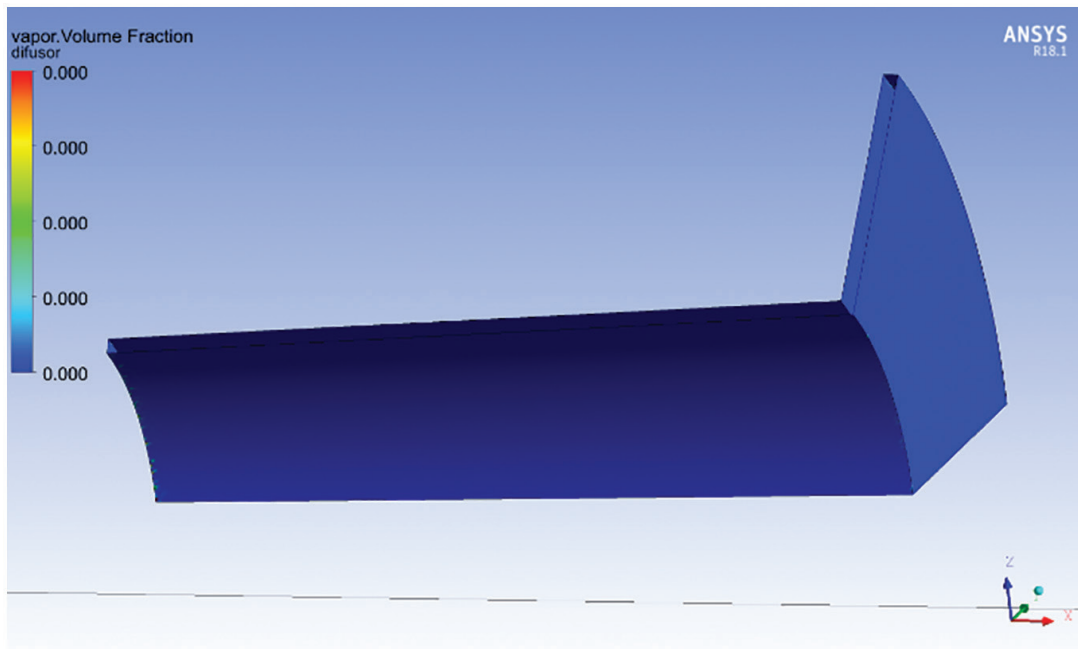
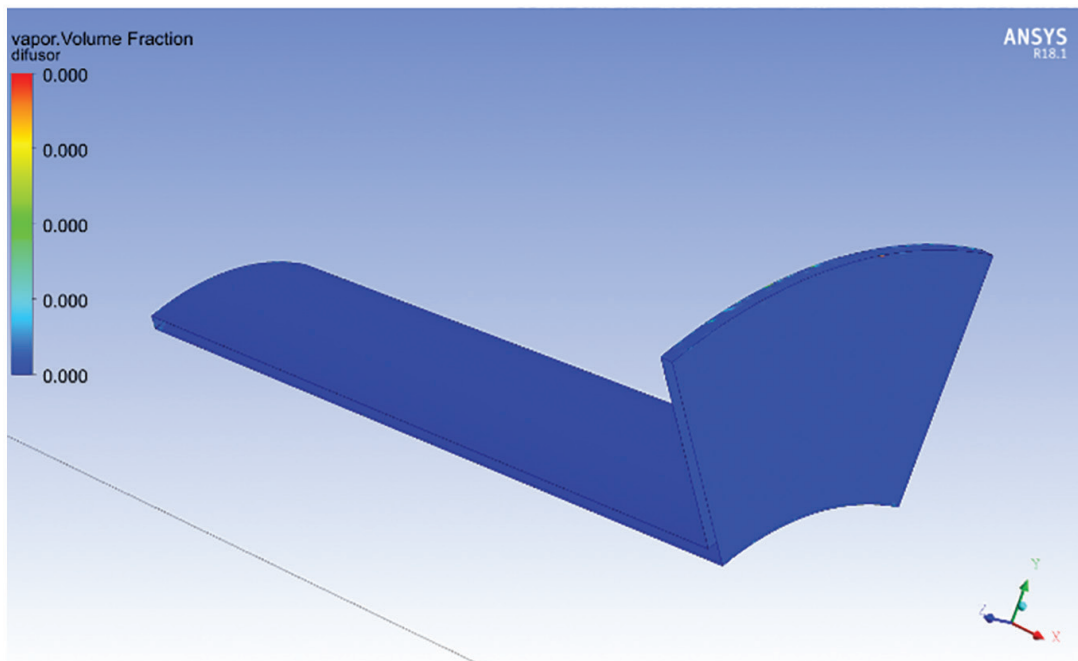**Figure 10:** Volume fraction of vapor on the diffuser inner part (a) and on the flange (b) for a immersion depth $H = 2.0$ m.

Figure 11: Pressure (a) and velocity magnitude (b) fields on the flanged diffuser for a $H = 3.0$ m depth.

Figure 12: Volume fraction of vapor on the diffuser inner part (a), and on the flange (b) for *H* = 3.0 m depth.

About the analysis performed on the fillet radius, it is observed that the bigger the fillet radius, the lower the stress. The radius of 14 mm was chosen because from it a low variation in stresses was observed. Thus, the dimensions selected for manufacturing the diffuser were 7 mm thickness with a fillet radius of 14 mm. This combination resulted in a safety factor of 3.45. A high safety factor was established as a criterion to prevent possible damage mechanisms not considered in this analysis as, for example, corrosion, possible welding problems, residual stresses, and fatigue. It is possible to work with thinner thicknesses by using structural reinforcements such as ribs in the flange to reduce the effects of bending.
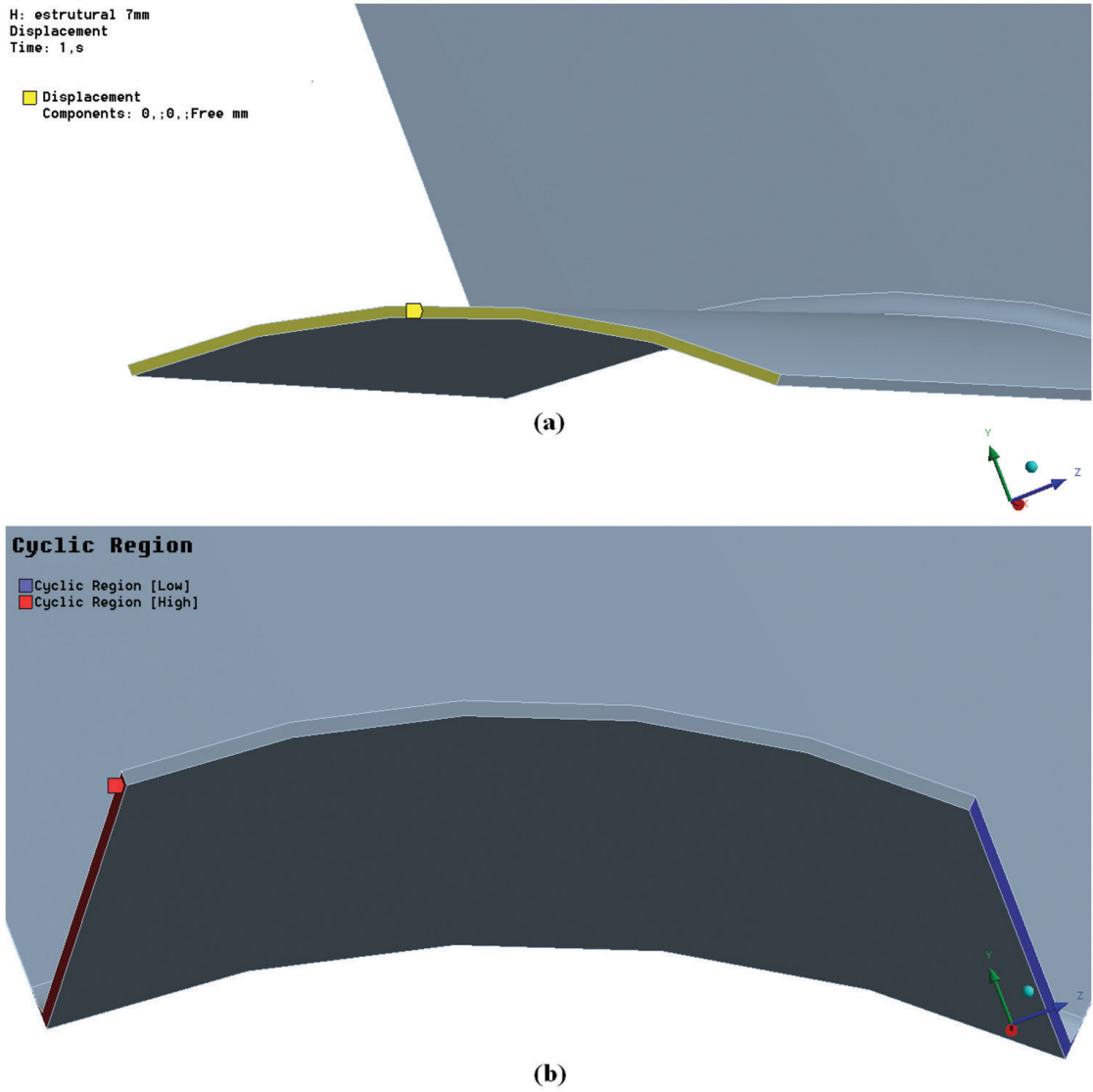
Figure 13: Boundary conditions: Fixed displacement applied on the diffuser front part (a) and Cyclic symmetry (b) on diffuser sides.
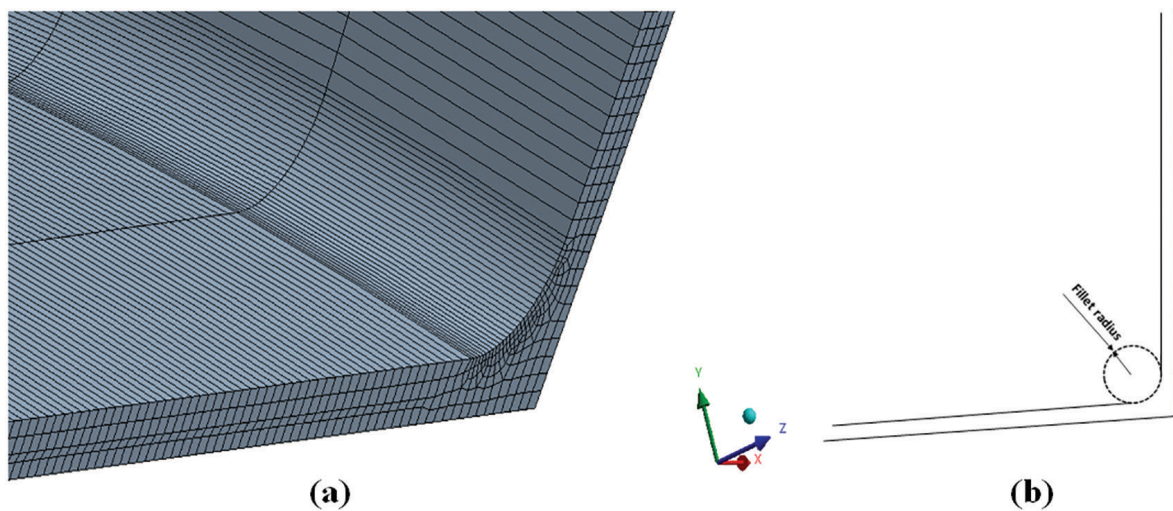

Figure 14: a) Mesh detail in the critical zone; (b) representation of the fillet radius at the flange junction with the diffuser.
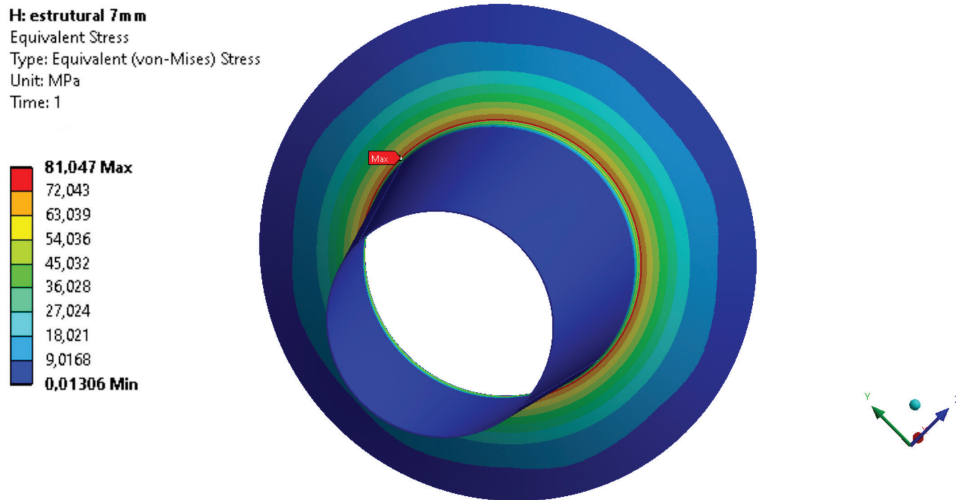
H: estrutural 7mm
Equivalent Stress
Type: Equivalent (von-Mises) Stress
Unit: MPa
Time: 1

81,047 Max
72,043
63,039
54,036
45,032
36,028
27,024
18,021
9,0168
0,01306 Min

Figure 15: Equivalent von-Mises Stress on the diffuser with 7 mm thickness.

Table 5: Stress analysis and Safety Factor in function of diffuser thickness and the fillet radius for 7 mm thickness.

FILLET RADIUS (mm)	THICKNESS (mm)	MAX. VON MISES STRESS (MPa)	SAFETY FACTOR
14	4	255.8	1.09
	6	110.9	2.52
	8	59.9	4.67
5	7	96.5	2.9
7		87.5	3.2
9		86.2	3.25
10		85.0	3.29
12		83.5	3.35
14		81.0	3.45

4. CONCLUSIONS

In this work, a numerical methodology was developed for cavitation and structural analysis on diffusers applied to hydrokinetic turbines. Only 1/8 of the geometry by applying periodicity on the sides of the domain in the CFD analysis was used, as well as a cyclic symmetry in the structural analysis was employed. Reynolds Averaged Navier Stokes (RANS) approach was used to evaluate the flow and the velocity at the central axis of the diffuser. It was compared with the experimental results of [17]. The turbulent viscosity ratio in the boundary layer near the diffuser wall was verified and found appropriate for the $\kappa - \omega - $ SST turbulence model. Cavitation was analyzed by applying the Rayleigh-Plesset model to estimate the rate of vapor production and a structural analysis was performed considering the von Mises failure criteria. The main findings and implications of the work are:

- The results obtained showed that cavitation occurs more intensely at a depth of 1.0 m for the model with diameter $D = 10$ m. This intensity gradually decreases as the depth increases.
- The dimensions selected for manufacturing the diffuser were 7 mm thickness with a fillet radius of 14 mm. This combination resulted in a safety factor of 3.45, which can be considered high, but it was established as a criterion to prevent possible damage mechanisms not considered in this analysis as, for example, corrosion, possible welding problems, residual stresses, and fatigue. However, Table 5 provides other geometric configurations with smaller factors, which can be used in other designs.
- Cavitation can be present in flanged diffusers, especially in the region inside the shroud, where it can directly impact the flow through the rotor. Also, especially in flanged diffuser, the effects of drag can induce high levels of stresses on the flange, so it is needed attention when this structure is constructed.

Defining the minimum thickness of the diffuser structure is fundamental for the design of flanged diffusers applied to hydrokinetic turbines. These results demonstrate that combining the study of cavitation with structural analysis is important for the proper design of flanged diffusers applied to axial axis hydrokinetic turbines.

5. ACKNOWLEDGMENTS

6. BIBLIOGRAPHY

[1]   IBRAHIM, W., MOHAMED, M.R., ISMAIL, R.M.T.R., *et al.,* "Hydrokinetic energy harnessing technologies: a review", *Energy Reports*, v. 7, pp. 2021–2042, 2021. doi: http://dx.doi.org/10.1016/j.egyr.2021.04.003.

[2]   REZEK, T., CAMACHO, R.G.R., MANZANARES FILHO, N.M., *et al.,* "Design of a hydrokinetic turbine diffuser based on optimization and computational fluid dynamics", *Applied Ocean Research*, v. 107, pp. 102484, 2021. doi: http://dx.doi.org/10.1016/j.apor.2020.102484.

[3]   Gaden, D.L.F., Bibeau, E.L., "A numerical investigation into the effect of diffusers on the performance of hydro kinetic turbines using a validated momentum source turbine model", *Renewable Energy*, v. 35, n. 6, pp. 1152–1158, 2010. doi: http://dx.doi.org/10.1016/j.renene.2009.11.023.

[4]   PICANÇO, H.P., LIMA, A.K.F., RIO VAZ, D.A.T.D., *et al.,* "Cavitation inception on hydrokinetic turbine blades shrouded by diffuser", *Sustainability*, v. 14, n. 12, pp. 7067, 2022. doi: http://dx.doi.org/10.3390/su14127067.

[5]   RIO VAZ, D.A., VAZ, J.R., SILVA, P.A., "An approach for the optimization of diffuser-augmented hydrokinetic blades free of cavitation", *Energy for Sustainable Development*, v. 45, pp. 142–149, Aug. 2018.

[6]   Gemaque, M.L.A., Vaz, J.R.P., SAAVEDRA, O.R., "Optimization of hydrokinetic swept blades", *Sustainability*, v. 14, n. 21, p. 13968, 2022. doi: http://dx.doi.org/10.3390/su142113968.

[7]   OWIS, F.M., "Numerical Investigation of loaded and unloaded diffuser equipped with a flange", *International Journal of Scientific and Engineering Research*, v. 6, n. 11, pp. 312–341, 2015.

[8]   HU, J.-F., WANG, W.-X., "Upgrading a shrouded wind turbine with a self-adaptive flanged diffuser", *Energies*, v. 8, n. 6, pp. 5319–5337, 2015. doi: http://dx.doi.org/10.3390/en8065319.

[9]   LELOUDAS, S.N., LYGIDAKIS, G.N., ESKANTAR, A.I., *et al.,* "A robust methodology for the design optimization of diffuser augmented wind turbine shrouds", *Renewable Energy*, v. 150, pp. 722–742, May. 2020. doi: http://dx.doi.org/10.1016/j.renene.2019.12.098.

[10]   BENJANIRAT, S., SANKAR, L., XU, G., "Evaluation of turbulence models for the prediction of wind turbine aerodynamics", In: *Proceedings of Wind Energy Symposium*, pp. 73–83, American Society of Mechanical Engineers (ASME), Jan. 2003.

[11]   LANZAFAME, R., MAURO, S., MESSINA, M., "Wind turbine CFD modeling using a correlation-based transitional model", *Renewable Energy*, v. 52, pp. 31–39, Apr. 2013. doi: http://dx.doi.org/10.1016/j.renene.2012.10.007.

[12]   MENTER, F.R., "Two-equation eddy-viscosity turbulence models for engineering applications", *AIAA Journal*, v. 32, n. 8, pp. 1598–1605, Aug. 1994. doi: http://dx.doi.org/10.2514/3.12149.

[13]   PLESSET, M.S., PROSPERETTI, A., "Bubble dynamics and cavitation", *Annual Review of Fluid Mechanics*, v. 9, n. 1, pp. 145–185, Jan. 1977. doi: http://dx.doi.org/10.1146/annurev.fl.09.010177.001045.

[14]   ŽNIDARČIČ, A., METTIN, R., DULAR, M., "Modeling cavitation in a rapidly changing pressure field: application to a small ultrasonic horn", *Ultrasonics Sonochemistry*, v. 22, pp. 482–492, Jan. 2015. doi: http://dx.doi.org/10.1016/j.ultsonch.2014.05.011. PubMed PMID: 24889548.

[15]   LINDAU, J.W., MORGUT, M., NOBILE, E., "Numerical predictions of cavitating flow around model scale propellers by CFD and advanced model calibration", *International Journal of Rotating Machinery*, v. 2012, pp. 618180, 2012.

[16]   BAKIR, F., REY, R., GERBER, A.G., *et al.,* "Numerical and experimental investigations of the cavitating behavior of an inducer", *International Journal of Rotating Machinery*, v. 10, n. 1, pp. 690740, 2004. doi: http://dx.doi.org/10.1155/S1023621X04000028.

[17]   FRANK, T., LIFANTE, C., JEBAUER, S., *et al.,* "CFD simulation of cloud and tip vortex cavitation on hydrofoils", In: *Proceedings of the 6th International Conference on Multiphase Flow (ICMF 2007)*, pp. 1–13, Paper No 134, Leipzig, Aug. 2007.

[18] GERBER, A.G., "A CFD model for devices operating under extensive cavitation conditions", In: *Proceedings of ASME 2002 International Mechanical Engineering Congress and Exposition (IMECE)*", pp. 341–349, Paper No: IMECE2002-39315, ASMEDC, Nov. 2002. doi: http://dx.doi.org/10.1115/IMECE2002-39315.

[19] ABE, K.-I., OHYA, Y., "An investigation of flow fields around flanged diffusers using CFD", *Journal of Wind Engineering and Industrial Aerodynamics*, v. 92, n. 3, pp. 315–330, Mar. 2004. doi: http://dx.doi.org/10.1016/j.jweia.2003.12.003.

[20] SILVA, P.A.S.F., SHINOMIYA, L.D., OLIVEIRA, T.F., *et al.,* "Analysis of cavitation for the optimized design of hydrokinetic turbines using BEM", *Applied Energy*, v. 185, pp. 1281–1291, Jan. 2017. doi: http://dx.doi.org/10.1016/j.apenergy.2016.02.098.

[21] ANSYS INC., *ANSYS CFX Fluent Users Guide. Release* 18.1, 2018.

[22] CUSTÓDIO FILHO, S.S., "Fatigue life estimation of hydrokinetic turbine blades", *Journal of the Brazilian Society of Mechanical Sciences and Engineering*, v. 42, n. 6, pp. 281, May. 2020. doi: http://dx.doi.org/10.1007/s40430-020-02372-9.

[23] SHINOMIYA, L.D., "*Design of horizontal axis hydrokinetic rotors considering the effect of cavitation* [Projeto de rotores hidrocinéticos de eixo horizontal considerando o efeito de cavitação]", Tese de M.Sc., Graduate Program in Mechanical Engineering, Institute of Technology, Federal University of Pará, Brazil, 2015.